Direct growth of SnO_2 nanocrystallites on electrochemically exfoliated graphene for lithium storage

Zexuan Xu,[a] Wenbo Yue,[a,*] Rong Lin,[a] Chang-Yang Chiang,[b] Wuzong Zhou[b,*]

[a] Beijing Key Laboratory of Energy Conversion and Storage Materials, College of Chemistry, Beijing Normal University, Beijing, 100875, China.

[b] School of Chemistry, University of St Andrews, St Andrews, Fife KY16 9ST, United Kingdom.

Abstract

As a new generation of high quality graphene, electrochemically exfoliated graphene is an ideal platform for constructing integrated high-performance nanocomposites as advanced electrode materials for energy storage and conversion devices. To take on a challenge of direct growth of nanoparticles on electrochemically exfoliated graphene with limited oxygen-containing functional groups and its hydrophobic nature, a systematic study is carried out on growth of SnO_2 nanocrystallites on the surface of electrochemically exfoliated graphene. The results indicate that these nanocrystals can efficiently grow on the functional group-free surface of electrochemically exfoliated graphene, if the precursor molecules can polymerize into larger molecules and aggregate on electrochemically exfoliated graphene followed by decomposition and phase transformation into the final metal oxide nanocrystallites. Some key factors affecting this non-classical crystal growth are investigated. Addition of a small amount of water in a polar aprotic solvent to stimulate polymerization of the precursor molecules and a solvothermal treatment to facilitate decomposition of the disordered

---

*Corresponding author. Tel.: +86 10 58804229; Fax: +86 10 58802075.
E-mail address: wbyue@bnu.edu.cn (W.B. Yue), wzhou@st-andrews.ac.uk (W.Z. Zhou)

aggregates of the polymerized precursors are crucial to the growth of nanocrystals on electrochemically exfoliated graphene. The improved electrical conductivity and structural stability of the hybrids may promote the performance of the materials in various applications, such as exceptional lithium storage capability.

Keywords: electrochemically exfoliated graphene, tin dioxide, polymerization, crystal growth, lithium-ion battery

1. Introduction

Since 2004, graphene has attracted wide attention due to its outstanding electrical, mechanical, thermal and optical properties [1,2]. Integration of graphene with various functional materials may promote their performance in some applications, such as exceptional lithium storage capability and electrocatalytic activity [3-5]. Although most of metal oxides possess high theoretical capacities (*e.g.* SnO_2: 782 mA h g^{-1}) [6,7], the low electronic conductivity and severe volume change of metal oxides during cycling seriously hinder their practical application in lithium-ion batteries (LIBs) [8,9]. Integration with graphene can enhance the electronic conductivity of the composites and effectively buffer the strain from the volume variation of metal oxides, leading to the improved electrochemical performance [10-12].

To date, graphene has been generated by several synthetic routes, including exfoliation of graphite through mechanical, chemical or electrochemical processes, growth of graphene nanosheets on substrates (*e.g.* chemical vapor deposition, SiC decomposition) and organic synthesis [13-15]. The pristine graphene has an inert surface with few active oxygen-containing groups. On the contrary, graphene oxide (GO) generated by chemical exfoliation of graphite contains many oxygen-containing functional groups on the surface (carboxyl, hydroxyl, carbonyl and epoxide groups) [16,17]. Accordingly, functional nanoparticles can be directly formed or anchored on the surface of GO by creating covalent bonds (*e.g.* grafting) or noncovalent interactions (*e.g.* electrostatic interactions) [18,19]. However, the electrical conductivity of GO is much lower than pristine graphene. Although the residual functional groups of GO in hybrids can be largely removed by thermal or chemical reduction, the electrical conductivity of the reduced graphene oxide (rGO) is still not comparable to that of pristine graphene due to a large number of surface defects [20].

Recently, mass production of high-quality graphene with a large lateral size has been achieved through a modified electrochemical exfoliation method [21,22]. Relatively fewer defects and higher electrical conductivity of these electrochemically exfoliated graphene (EEG) make it more suitable to replace rGO as building component for the construction of graphene hybrids, which may exhibit better performance than rGO-based composites. However, lack of oxygen-containing surface groups makes it more difficult to anchor or grow functional nanoparticles on the surface. Furthermore, EEG can only be dispersed in polar aprotic solvents (*e.g.* N,N-dimethylformamide, DMF) due to its inert surface and hydrophobic nature, limiting the synthesis conditions [21].

Up to now, there are few researches on the fabrication of EEG hybrids and on their physico-chemical properties in spite of their potential wide applications. Some rare examples revealed difficulties of preparing the EEG hybrids in some conventional methods. Feng's group described a typical assembly of EEG hybrids (Si, Fe_3O_4 and Pt nanoparticles) with a sandwich-like structure [23]. According to their report, polyaniline acted as a versatile dopant to couple nanoparticles onto EEG through electrostatic interactions or hydrogen bonding. However, such a complicated noncovalent linkage of nanoparticles- polyaniline-EEG would reduce the electrical conductivity and chemical stability of the EEG hybrids. EEG-based metal oxides (*e.g.* Fe_2O_3) can also be obtained by electrochemical exfoliation of graphite in electrolyte solution containing metal oxide precursors (*e.g.* $FeSO_4$) [24,25]. The whole process includes alternating deposition of metal oxides onto the surface of graphite electrodes and exfoliation of outer graphene layer attached with the metal oxides. However, the gradual change in concentration of electrolyte solution may cause the non-uniformity of nanocrystal-decorated EEG. In addition, to avoid stacking of EEG in water, nickel foam supported EEG or EEG foils were selected to fabricate the EEG hybrids [26,27]. It is true that a simple and facile methodology for growing functional nanoparticles on EEG, especially in polar aprotic solvents, is yet to be developed.

In the present work, a new method is proposed, in order to overcome the inert property of the EEG surface. We try to introduce oxygen-containing active groups into the precursor molecules and allow them to polymerize into larger molecules, which can be adsorbed on the EEG surface via multiple interaction sites. Nucleation and crystal growth then occur in the adsorbed precursor aggregates. A systematic study has been carried out on the direct growth of SnO_2 functional nanocrystals on the surface of EEG in a polar aprotic solvent (DMF), as an example to demonstrate this crystal route. The new mechanism of crystal growth is investigated in detail. The advantages of the EEG hybrids in comparison with rGO hybrids are discussed, in particular, about their outstanding electrochemical performance, such as exceptional lithium storage capability. This novel and facile method for the synthesis of EEG-supported metal oxides offers a great promise for the development of advanced EEG hybrids utilized in various applications.

2. Experimental

2.1 Sample preparation

EEG, GO and rGO. EEG and GO were synthesized according to the published literature (see the Supporting Information for details) [21,28]. rGO was produced by reduction of GO. In a typical preparation, 0.1 g of GO was dispersed into 75 mL of distilled water under ultrasonication. The solution was then transferred into a 100 mL Teflon-lined stainless steel autoclave and maintained at 160°C for 12 h. GO was reduced to rGO during this hydrothermal process. The product was collected by centrifugation, washed with distilled water, and dried at 60°C.

EEG-SnO_2. In a typical synthesis, 0.03 g of EEG was dispersed in 60 ml of DMF under ultrasonication for 1 h. 0.16 g of $SnCl_4{\cdot}5H_2O$ and a small amount of distilled water (0.1, 0.3 or 0.5 mL) were added to the above suspension. After stirring for 20 min, the mixture was transferred into a 100 ml Teflon-lined stainless steel autoclave and maintained at 160°C for 12 h. After cooling down to room temperature, the product was collected by centrifugation, washed with ethanol and distilled water, and dried at 60°C. For comparison, EEG-SnO_2 was also prepared under the same synthesis conditions except without addition of water or solvothermal treatment at 100°C, instead of 160°C, for 12 h.

rGO-SnO_2. In a typical synthesis, 0.1 g of GO was dispersed into 75 mL of distilled water under constant ultrasonication. 0.074, 0.106 or 0.146 g of $SnCl_4{\cdot}5H_2O$ was then added into the GO suspension with vigorous stirring for 20 min. Subsequently, the suspension was transferred into a 100 mL Teflon-lined stainless steel autoclave and maintained at 160°C for 12 h. The product was collected by centrifugation, washed with distilled water, and dried at 60°C.

2.2 Sample characterisation

Specimens were characterized by the following techniques. X-ray diffraction (XRD) was performed on a Phillips X'pert Pro MPD diffractometer with Cu Kα radiation. The Fourier transform infrared (FT-IR) was performed on a Nicolet-380 Fourier-transform infrared spectrometer in the range of 400-4000 cm^{-1}. X-ray photoelectron (XPS), was carried out on a Shimadzu Axis Ultra spectrometer with an Mg Kα = 1253.6 eV excitation source, Raman scattering spectra were recorded on a Jobin-Yvon Laser Confocal Micro-Raman Spectrometer with a 633 nm laser source. The elemental analysis for C, H and N contents was performed on a LabRAM ARAMIS analyzer. Mass spectra were obtained on an AB Sciex TripleTOF 5600™ mass spectrometer. The thermogravimetric analysis (TGA) was carried out on a NETZSCH STA 409 PC/PG thermal analyzer and carried out in air at a heating rate of 5°C min^{-1}. Transmission electron microscopy (TEM) and high-resolution TEM (HRTEM) images were recorded on a JEOL JEM-2011 electron microscope and a FEI Titan Themis electron microscope, both operated at 200 kV. Scanning electron microscope (SEM) and energy-dispersive X-ray microanalysis (EDX) were performed on a JEOL JSM-6700F electron microscope at an accelerating voltage of 5 kV.

2.3 Electrochemical measurement

The electrochemical performance of specimens were tested using a LR2032-type coin cell. The lithium metal was used as the negative electrode. The positive electrode was prepared by mixing the specimens, Super P carbon black and polyvinylidene difluoride (PVDF) dissolved in N-methyl-2-pyrrolidine (NMP) in a weight ratio of 80 : 10 : 10. The mixed slurry was pressed onto a copper foil and dried at 110°C in vacuum for 24 h. The electrolyte was 1 M solution of $LiPF_6$ dissolved in a EC : DEC : DMC solution with a 1 : 1 : 1 vol ratio. Cell assembly was carried out in an Ar-filled glove box. The area of the electrode was 2.0 cm^2 and the mass loading of active materials was about 2.5 mg cm^{-2}. Cyclic voltammetry tests were performed between 0.01 and 3.0 V with a scan rate of 0.5 mV s^{-1}. The galvanostatic charge-discharge tests were performed on a LAND test system at room temperature, and the voltage range was from 0.01 to 3.0 V (versus Li/Li^+), with a constant current of 0.1–2 C (1 C equals to the theoretical capacity of SnO_2, 782 mA h g^{-1}). The electrochemical impedance spectroscopy (EIS) was carried out in the frequency range from 100 kHz to 10 mHz on a Gamry Interface 1000 electrochemical station. The electrical conductivity of samples were measured by a four point probe set up from a Keithley 2400 source meter.

3. Results and discussion

3.1 EEG and rGO

EEG was produced using a modified electrochemical exfoliation method, which offers high quality graphene with a large lateral size (**Fig. 1a**) [21]. For comparison, conventional rGO was prepared via hydrothermal reduction of GO. The details of the synthetic methods of these specimens and all other samples are given in the Experimental Section.

It can be expected that EEG has less oxygen-containing functional groups and defects on the surface, and thereby presents higher electrical conductivity than rGO. The surface structures of GO, rGO and EEG were studied by using FT-IR, XPS and Raman spectroscopies.

Compared to the FT-IR spectrum of GO, the C–O and C=O bands disappear and the intensity of C–OH band decreases sharply in the FT-IR spectrum of rGO (**Fig. S1a** in Supporting Information). Moreover, the intensity ratio of C 1s peak to O 1s peak significantly increases in the XPS spectrum of rGO (**Fig. S1b**), indicating that most oxygen-containing functional groups of GO (*e.g.* carboxyl and carbonyl groups) have been removed by the hydrothermal treatment [29]. The C 1s peak in the high resolution XPS spectrum (**Fig. S1c**) can be further resolved into four components, corresponding to C–C (~284.6 eV), C–O (~286.6 eV), C=O (~287.6 eV) and O–C=O (~288.8 eV) groups, respectively. The peaks related to oxygen-containing groups (C–O, C=O and O–C=O) almost disappear in the XPS spectrum of rGO, which is consistent with the FT-IR result [30]. Similarly, there is few oxygen-containing functional groups on the surface of EEG, confirmed by FT-IR and XPS (**Fig. S1a-c**). The C/O molar ratios of EEG and rGO determined by CHN analysis (**Table S1**) are 7.68 and 5.64 respectively, much higher than that of GO (1.28) [31].

In the Raman spectra (**Fig. S1d**), the D band around 1346 cm^{-1} is related to the vibration of sp^3 carbon atoms of disordered graphite, and the G band around 1590 cm^{-1} is related to the in-plane vibration of sp^2 carbon atoms in a 2D hexagonal lattice [32]. The intensity ratio of the D band and G band (I_D/I_G) of rGO (0.98) is very close to that of GO (1.13), reflecting that many defects remain on the surface of rGO after removal of the oxygen-containing groups. On the contrary, EEG possesses much less defects on the surface ($I_D/I_G = 0.32$), guaranteeing a fast electron transport.

A four point probe technique was used to measure the electrical conductivity of samples (**Table S2**) [33]. The electrical conductivity of EEG film is 240.4 S cm^{-1}, much higher than that of rGO (29.0 S cm^{-1}). Therefore, EEG is more suitable to be used as graphene substrate than rGO, and fabrication of EEG-supported nanomaterials is of great interest for developing advanced electrodes with excellent electrochemical or electrocatalytic performance. However, as mentioned above, it remains challenging to anchor or grow nanocrystallites on the surface of EEG due to its limited surface functional groups. Furthermore, EEG can only be dispersed in polar aprotic solvents (*e.g.* DMF) due to its hydrophobic nature and inert surface property, further hindering the synthesis processing. As shown in **Fig. 1b**, GO can be dispersed in water, while EEG can be dispersed evenly in DMF, but not in water.

3.2 EEG-SnO_2 and rGO-SnO_2

EEG-based SnO_2 nanocomposites (EEG-SnO_2) were successfully prepared in DMF solvent through a solvothermal method. For comparison, rGO-based SnO_2 nanocomposites (rGO-SnO_2) were also prepared by using a hydrothermal method. All the peaks in the XRD patterns of EEG-SnO_2 and rGO-SnO_2 (**Fig. 1c**) are indexed into the tetragonal structure of SnO_2 (space group P_{42}/mnm) and no crystalline impurities are detected. The broadness of the peaks indicate that the SnO_2 crystallites in both samples are quite small.

SEM and TEM images of EEG-SnO_2 (**Fig. 1d,e**) reveal that SnO_2 nanocrystallites with a diameter of 2~3 nm are well-distributed on the surface of EEG without obvious aggregation. HRTEM image (**Fig. 1f**) further confirms that the ultrathin EEG substrate (triple-layer graphene as seen at the curled edge) is decorated with SnO_2 nanocrystallites. A *d*-spacing is measured from the observed fringes on a nanocrystallite to be ~0.335 nm, in a good agreement with the interplanar spacing of the (110) planes of the SnO_2 crystalline structure. Comparing with the SEM and TEM images of rGO-SnO_2 (**Fig. S2a-c**), there is no obvious difference in crystal size, morphology and dispersibility of the SnO_2 nanocrystallites between EEG-SnO_2 and rGO-SnO_2.

Furthermore, TGA curves (**Fig. S2d**) show that the content of SnO_2 in EEG-SnO_2 is 32.9 wt%, even slightly larger than the value in rGO-SnO_2 (31.5 wt%), further confirming the similarity of the deposition of SnO_2 nanocrystallites on both EEG and rGO. Therefore, any possible difference in the electrochemical properties of these hybrids would mainly depend on the quality of graphene substrates.

The crystallinity of EEG and rGO in the composites was also characterized by HRTEM. The characteristic hexagonal atomic lattices of graphene are clearly observed around SnO_2 crystals in the HRTEM image of EEG-SnO_2 (**Fig. 2a**). The lattice spacing of ~0.21 nm is assigned to the (100) planes of graphite [34]. On the contrary, rGO shows much poor ordering in the crystal structure compared to EEG (**Fig. 2b**), indicating that many defects formed after removal of oxygen-containing groups [35]. It is noted that a group of fringes of the SnO_2 nanocrystal in **Fig. 2a** is parallel to the (100) fringes of the EEG substrate, implying that the connection of the two components is more likely covalent.

FT-IR and C 1s XPS spectra of rGO-SnO_2 (**Fig. 2c,e**) reveal that most oxygen-containing groups of GO have been removed during the hydrothermal synthesis. However, according to the high I_D/I_G value of rGO-SnO_2 (1.08) in the Raman spectrum (**Fig. 2f**), many defects are remained on the surface of rGO, which is consistent with HRTEM observation. In contrast to rGO-SnO_2, less oxygen-containing groups are present in EEG-SnO_2 according to the higher intensity ratio of C 1s peak to O 1s peak (**Fig. 2d**). Besides, the I_D/I_G of EEG-SnO_2 is 0.60, much lower than that of rGO-SnO_2 (1.08). As a consequence, EEG-SnO_2 has much higher electrical conductivity (40.5 S cm^{-1}) than rGO-SnO_2 (20.7 S cm^{-1}) (**Table S2**). On the other hand, the I_D/I_G of pristine EEG is 0.32, lower than that of EEG-SnO_2 (0.60). It is an evidence to demonstrate that the growth of SnO_2 nanocrystals leads to generation of additional defects on the surface of EEG. In other words, many original sp^2-type carbon atoms underneath the SnO_2 nanocrystallites have changed to sp^3-type via formation of C-O-Sn bonds. The Sn-O band in the FT-IR spectrum (**Fig. 2c**) and the Sn 3d peak in the XPS spectrum (**Fig. 2d**) verify the formation of SnO_2 on the surfaces of EEG and rGO.

Graphene-based functional materials are deemed as promising electrode materials for energy storage and conversion devices, such as LIBs and DMFCs. Accordingly, cyclic voltammetry and galvanostatic charge/discharge tests were performed to evaluate the electrochemical performance of EEG-SnO_2 and rGO-SnO_2. The CV curve of EEG-SnO_2 (**Fig. 3a**) in the first cycle shows one pair of peaks at 0.68/1.33 V, corresponding to the conversion reaction

$$SnO_2 + 4Li^+ + 4e^- \leftrightarrow Sn + 2Li_2O \quad (1)$$

and one pair of peaks at 0.16/0.72 V, corresponding to the alloying and dealloying reaction [36,37]

$$Sn + xLi^+ + xe^- \leftrightarrow Li_xSn,\ 0 \leq x \leq 4.4. \quad (2)$$

The reduction peaks shift to 1.03 V in the subsequent cycles owing to the polarization of the electrode. The subsequent scans almost overlap with each other, reflecting a good reversibility of EEG-SnO_2. **Fig. S3** depicts voltage profiles of EEG-SnO_2 and rGO-SnO_2 for the 1st, 2nd, 10th and 50th charge/discharge cycles. Four voltage plateaus at ca. 0.2, 0.6, 1.0 and 1.3 V are observed, which are consistent with the CV results.

The cycle and rate performance of EEG-SnO_2 and rGO-SnO_2 are shown in **Fig. 3b,c**. The reversible capacity of rGO-SnO_2 decreases dramatically after 40 cycles, and only 516 mA h g^{-1} is achieved at 0.1 C after 100 cycles. In contrast, EEG-SnO_2 exhibits excellent cycling stability, and a capacity of 917 mA h g^{-1} is achieved at 0.1 C after 100 cycles, which corresponds to 103% capacity retention versus the second cycle (894 mA h g^{-1}). When the current density increases to 2 C, the reversible capacity of EEG-SnO_2 decreases to 495 mA h g^{-1}, still much higher than that of rGO-SnO_2 (293 mA h g^{-1}). When the current density returns to 0.1 C, a capacity of 900 mA h g^{-1} is recoverable, demonstrating the good cycling stability of EEG-SnO_2. It is worth noting that the initial capacity of EEG-SnO_2 (1380 mA h g^{-1} at 0.1 C) (Fig. 3b) is much higher than the theoretical capacity of SnO_2, which can be attributed to the formation of a solid electrolyte interface (SEI) film on the surface of EEG-SnO_2. The formed SEI films also result in large irreversible capacity losses in the initial cycles. Some methods such as fabrication of TiO_2 nanofilms on the surface of graphene-SnO_2 can be employed to reduce its irreversible capacity [38].

As a high-quality graphene substrate, EEG can offer higher electronic conductivity and stronger mechanical strength than rGO in graphene-based composites, which may highly improve the lithium storage capability of the composites. To evaluate the electron transfer rate in the composites, electrochemical impedance spectroscopy (EIS) measurements of EEG-SnO_2 and rGO-SnO_2 were performed after 3 cycles. **Fig. 3d** shows the Nyquist plots consisting of two overlapping semicircles in the high and medium frequency range, which reflect the migration of the Li^+ through the SEI film (R_f) and the charge transfer resistance (R_{ct}), and a sloping straight line in the low frequency range, which reflects the diffusion properties of Li^+ in solid materials (Z_w) [39]. Apparently, the diameter of the semicircle for EEG-SnO_2 is much smaller than that for rGO-SnO_2, indicative of a lower contact and charge transfer resistances of EEG-SnO_2. Based on a Randles equivalent circuit model (the inset of **Fig. 3d**), the R_f and R_{ct} values of EEG-SnO_2 are calculated to be 3.7 and 11.8 Ω, respectively (**Table S2**), smaller than those of rGO-SnO_2 (4.7 and 18.5 Ω).

The structure and morphology of these samples after 100 cycles were also examined using TEM. The aggregation of Sn/SnO_2 nanocrystallites (Sn is produced according to equ. 1) is inevitable on the rGO substrate in view of severe SnO_2 volume change and particle movement during cycling (**Fig. S4a**), whereas separated Sn/SnO_2

nanocrystallites are preserved on the EEG substrate (**Fig. S4b**). The long-term structural stability of EEG-SnO_2 may be attributed to the outstanding mechanical properties of EEG [40], which effectively relieve the stress caused by the volume variation of SnO_2. The improved electrical conductivity and structural stability of EEG-SnO_2 is conducive to improving the electrochemical performance of the electrodes.

3.3 Higher loading of SnO_2 on EEG and rGO

EEG-SnO_2 and rGO-SnO_2 with higher loadings of SnO_2 were also controllably synthesized and denoted as EEG/rGO-SnO_2-M (middle loading) and EEG/rGO-SnO_2-H (high loading). The TGA curves (**Fig. S5**) show that the content of SnO_2 is 52.6 wt% for EEG-SnO_2-M, 53.5 wt% for rGO-SnO_2-M, 66.0 wt% for EEG-SnO_2-H, and 65.3 wt% for rGO-SnO_2-H. The contents of SnO_2 in both EEG- and rGO-based specimens were controlled to be similar in order to investigate the comparative effects of two different types of graphene on the electrochemical performance of the electrodes. It is worth noting that the content of SnO_2 in rGO-SnO_2 can be simply adjusted by controlling the dosage of the Sn-containing precursor (*e.g.* $SnCl_4$) in water. However, the content of SnO_2 in EEG-SnO_2 cannot be merely adjusted by controlling the dosage of $SnCl_4$. For instance, when excessive $SnCl_4$ is present, the content of SnO_2 in EEG-SnO_2 increases with increasing the dosage of water in DMF, indicating that water plays an important role in the formation of SnO_2.

SEM and TEM images of EEG-SnO_2-M and EEG-SnO_2-H (**Fig. 4a-d**) reveal that most of SnO_2 nanoparticles are well-dispersed on the surface of EEG even at high loading of SnO_2, and few SnO_2 agglomerates inevitably form with the increase of SnO_2 content. It seems that more SnO_2 agglomerates obviously form on the surface of rGO with the increase of the SnO_2 content (**Fig. S6**), which may be attributed to the different crystal growth mechanism in water and in DMF.

Raman spectra (**Fig. 4e,f**) indicate that the I_D/I_G value increases from 0.60 of EEG-SnO_2 (**Fig. 2f**) to 0.74 of EEG-SnO_2-M and 0.90 of EEG-SnO_2-H, whereas the I_D/I_G of rGO-SnO_2 (1.08) is very similar to that of rGO-SnO_2-M (1.12) or rGO-SnO_2-H (1.10). It is reasonable to say that SnO_2 crystals grow on the surface of GO by reaction with the epoxy and hydroxyl groups to form C-O-Sn bonds [40], while the SnO_2 crystals grow directly on the carbon of EEG to create new defects. Consequently, the number of defects of the rGO substrate does not change much after the growth of SnO_2 crystals. When almost all the sites of the epoxy and hydroxyl groups in GO are occupied by SnO_2 crystals, the new nanoparticles may be developed near the existing nanocrystallites, leading to the particle aggregation. On the contrary, the increase of defects in EEG with the increase of the SnO_2 loading implies that the SnO_2 crystals can grow on the graphitic surface of EEG, free of the epoxy and hydroxyl groups. It is further confirmed that the sp^2 carbon atoms in a 2D hexagonal lattice change to sp^3 carbon atoms by forming C-O-Sn bonds after the growth of the SnO_2 crystals, resulting in the increase of defects in EEG. Since the nanocrystallites can grow anywhere on the EEG surface, its distribution become more even and the number of agglomerates can be greatly reduced.

To further verify the advantages of the EEG substrate for the electrodes, the electrochemical performance of EEG/rGO-SnO_2-M and EEG/rGO-SnO_2-H were studied by galvanostatic measurements. Although the theoretical capacity of SnO_2 (782 mA h g^{-1}) is slightly higher than that of graphene (744 mA h g^{-1}), the electrochemical performance of rGO-SnO_2 decreases considerably with the increase of SnO_2 content. As shown in **Fig. 5a,c**, rGO-SnO_2-M and rGO-SnO_2-H exhibit capacities of 438 and 298 mA h g^{-1} at 0.1 C after 100 cycles respectively, much lower than that of rGO-SnO_2 (516 mA h g^{-1}). At a high current density of 2 C (**Fig. 5b,d**), rGO-SnO_2-M and rGO-SnO_2-H deliver capacities of 214 and 175 mA h g^{-1} respectively, still lower than that of rGO-SnO_2 (290 mA h g^{-1}). The poor electrochemical performance of rGO-SnO_2 with high content of SnO_2 can be attributed to the heavy aggregation of SnO_2 nanoparticles as well as the increased resistances of the composites. The electrical conductivity of rGO-SnO_2-M and rGO-SnO_2-H is 15.8 and 10.0 S cm^{-1} respectively (**Table S2**), lower than that of rGO-SnO_2 (20.7 S cm^{-1}). Nyquist plots (**Fig. 5e,f**) also demonstrate that the R_{ct} value of the electrode increases from 18.5 Ω of rGO-SnO_2 to 20.1 Ω of rGO-SnO_2-M and 32.1 Ω of rGO-SnO_2-H.

On the contrary, EEG-SnO_2 shows a good cycling stability even at high loading of SnO_2. After 100 cycles at 0.1 C, the reversible capacities of EEG-SnO_2-M and EEG-SnO_2-H are maintained at 830 and 768 mA h g^{-1} respectively (**Fig. 5a,c**), much higher than those of rGO-SnO_2-M and rGO-SnO_2-H. As the current density increases to 2 C, EEG-SnO_2-M and EEG-SnO_2-H still deliver favorable capacities of 475 and 443 mA h g^{-1}, respectively (**Fig. 5b,d**). The good electrical conductivity and mechanical strength of EEG are beneficial to improving the electrochemical performance of the electrodes. Compared to rGO-SnO_2-M and rGO-SnO_2-H, EEG-SnO_2-M and EEG-SnO_2-H have higher electrical conductivity (28.3 and 18.8 S cm^{-1}, **Table S2**) and lower charge-transfer resistances (16.3 and 21.0 Ω) (**Fig. 5e,f**). It is believed that fewer SnO_2 agglomerates formed on the EEG substrate may also contribute to the superior electrochemical performance of the composites.

3.4 Growth Mechanism of SnO_2 on EEG.

To explore key factors affecting the crystal growth in DMF, EEG-SnO_2 was prepared under the same synthesis condition for EEG-SnO_2-H except no addition of water (referred to as EEG-SnO_2-NW, NW for no water addition) or reducing the temperature of the solvothermal reaction (referred to as EEG-SnO_2-LT, LT for low temperature). SEM images of EEG-SnO_2-NW and EEG-SnO_2-LT (**Fig. 6a,b**) demonstrate that small numbers of SnO_2 nanoparticles are present on the surface of EEG. The diffraction peaks corresponding to the stacking of graphene nanosheets instead of the crystal structure of SnO_2 are detected in the XRD patterns (**Fig. 6c**), implying low contents of SnO_2 in these samples. TGA curves (**Fig. 6d**) indicate that the contents of SnO_2 in EEG-SnO_2-NW and EEG-SnO_2-LT are only 15.8 and 13.3 wt%, respectively, much lower than that in EEG-SnO_2-H (66.0 wt%). Consequently, the addition of water and the solvothermal process play important roles on the formation and growth of SnO_2 crystals on the EEG substrate in DMF.

Recently, the formation mechanism of SnO_2 nanocrystallites in acidic ethanol solution was systematically studied [41]. It has been found that a mixture of tin chloride monomeric complexes composed of $[SnCl_5(H_2O)]^-$, $SnCl_4(H_2O)_2$ and $[SnCl_3(H_2O)_3]^+$ was present in the initial solution. After addition of water and aging at room temperature, polynuclear tin-oxo clusters with double- or triple-chain structures were formed and further interconnected to form SnO_2 nanoparticles. A densification of SnO_2 nanoparticles followed by an advanced nanocrystallite growth occurred during heating and aging at high temperature (70°C).

In the present work, the polynuclear tin-oxo clusters in DMF were also identified by mass spectroscopy, and water addition favors the formation of clusters. Besides tin chloride monomeric complexes of $[SnCl_3(H_2O)_3]^+$ and $SnCl_4(H_2O)_2$ *etc.*, some polymerized larger molecules were also detected in the mass spectrum. **Fig. S7** shows some typical examples, including dimmers $Sn_2Cl_2(OH)_6(H_2O)_2$, $Sn_2Cl_5(OH)_3(H_2O)_2$, trimer $Sn_3Cl(OH)_{11}(H_2O)_2$, and tetramer $Sn_4Cl_2(OH)_{14}(H_2O)_2$. The full mass spectrum is shown in **Fig. S8b**. The formation of the large polymerized molecules is extremely important in the growth of SnO_2 nanoparticles on EEG, since the inter-molecular interaction between the polymer molecules and EEG increases with the size of the molecules. As detected previously [23], the surface of EEG is negatively charged in DMF solvent. On the other hand, in the present work, the polymerized molecules are positively charged under an acidic condition (pH ~4). Consequently, the molecules intend to migrate to the surface of EEG driven by electrostatic interactions.

The polymerized molecules can further aggregate into larger clusters on the EEG surface due to strong intermolecular interaction. The clusters then decompose during the solvothermal treatment and crystallize into SnO_2 nanoparticles, which link to the EEG surface with multiple covalent bonds of C-O-Sn.

Consequently, the growth of SnO_2 nanocrystals on EEG does not follow the classical crystal growth route, *i.e.* starting with nucleation on the EEG surface and growth via layer-by-layer deposition of the building units, tin cations and oxide anions. We then proposed a new multistep mechanism, as illustrated in **Figure 7**. Step 1, $SnCl_4$ is hydrolyzed slowly in DMF with a small amount of water, forming monomer hydrolysates, $SnCl_3(OH)(H_2O)_2$ and $SnCl_2(OH)_2(H_2O)_2$ *etc*. Two or more such hydrolysates connect to form a dimer, trimer, tetramer or even larger tin chloride based polymerized clusters (**Fig. 7a**), as detected by mass spectroscopy. In fact, without addition of water, very small amount of large molecules were formed in the system (see **Fig. S8a**) and the formation of SnO_2 on the EEG surface became very difficult. Step 2, these polymer clusters deposit on the EEG surface through inter-molecular interactions or electrostatic interactions, and grow larger (**Fig. 7b**). Evidence of such deposition has been obtained from SEM, EDX and HRTEM (see further discussion below). Step 3, all the chloride ions will be dissociated in a process of surface hydrolysis. The resulted tin hydroxide undergoes further dehydration, decomposition and phase transformation into SnO_2 nanocrystallites during a solvothermal process. More likely, the particles link to carbon on the surface of EEG to form C-O-Sn bonds (**Fig. 7c**).

Crystallization of disordered aggregates of precursors is a common crystal growth route as seen in non-classical reversed crystal growth of many materials [42,43]. Although the growth of SnO_2 may also take place on defect sites including the sites of functional groups, it is not a principal route due to a small number of these active sites in EEG.

To further confirm the proposed mechanism, a few more experiments were performed. Solid specimens from the mixtures of EEG and $SnCl_4{\cdot}5H_2O$ in DMF before and after the solvothermal treatment were collected (referred to as EEG-$SnCl_4$ and EEG-SnO_2-Hx, respectively), and examined using SEM. In contrast to the pristine EEG with smooth surface, the surface of EEG-$SnCl_4$ adsorbs some loose and low density particles (**Fig. S9a**). The particles are likely aggregated polymer clusters. The Sn, O, Cl elements were detected in the EDX spectrum (**Fig. S9c**), also verifying the presence of polymer clusters on the EEG substrate. An HRTEM image showing polymerized precursor molecules on the EEG surface is shown in **Fig. S10**.

After the solvothermal treatment for a short time (0.5 h), SnO_2 nanocrystals (very small white spots) can be distinguished on the EEG surface (**Fig. S9b**), indicating that the solvothermal treatment is important to promote the hydrolysis process. The Cl element is hardly detected in the EDX spectrum of EEG-SnO_2-Hx (**Fig. S9d**), which is ascribed to the release of chlorine anions from the condensed SnO_2 nanoparticles. These nanoparticles are highly dispersed on the surface of EEG and no aggregation is observed. Thus we believe that SnO_2 nanocrystals can directly grow on the surface of EEG in absence of functional groups, but a certain amount of energy barriers need to be overcome (*e.g.* a solvothermal treatment is required) [44]. In addition, EEG alone is treated in DMF with water under solvothermal condition. The I_D/I_G of treated EEG does not change much in the Raman spectrum (not shown), illustrating that water cannot create the defects in EEG even under solvothermal treatment. The defects of EEG should be generated during the formation and growth of SnO_2 crystals.

4. Conclusions

In summary, we have developed a novel and facile method for the synthesis of SnO_2 nanocrystals on the surface of EEG in DMF. Unlike the classical growth route for metal oxides-decorated rGO, the formation of SnO_2 nanocrystals relies on phase transformation from metal-containing precursors to metal hydroxides and finally metal oxides via dehydration. Accordingly, the solvothermal process in DMF with addition of a small amount of water plays an important role on the growth of nanocrystals on EEG.

The EEG substrate used instead of rGO has several advantages for the performance improvement of the composites: (1) EEG exhibits better properties than rGO, such as higher electrical conductivity and stronger mechanical strength. (2) The newly generated defects of EEG caused by the growth of nanocrystals are limited, whereas a large number of defects have been already present on the surface of rGO, even at low loading of nanocrystals. (3) In contrast to the dispersed nanocrystals on the EEG substrate, nanocrystals tend to grow and aggregate on the defects of rGO. All the above factors are beneficial to improving the electrochemical or electrocatalytic performance of EEG hydrides. This novel strategy for integration of EEG with functional materials offers access to the development of advanced electrode materials for energy storage and conversion devices such as batteries and fuel cells.

Acknowledgements

This work was financially supported by National Natural Science Foundation of China (21573023). WZ thanks EPSRC's support to the electron microscopy Laboratory for a Capital Equipment Grant EP/L017008/1.

References

[1] K.S. Novoselov, A.K. Geim, S.V. Morozov, D. Jiang, Y. Zhang, S.V. Dubonos, I.V. Grigorieva, A.A. Firsov, Science 306 (2004) 666–669.

[2] A.K. Geim, K.S. Novoselov, Nat. Mater. 6 (2007) 183–191.

[3] D. Sun, D.L. Ye, P. Liu, Y.G. Tang, J. Guo, L.Z. Wang, H.Y. Wang, Adv. Energy Mater. 8 (2018) 1702383.

[4] R. Zhang, H.Y. Li, D. Sun, J.Y. Luan, X.B. Huang, Y.G. Tang, H.Y. Wang, J. Mater. Sci. 54 (2019) 2472–2482.

[5] S.K. Bikkarolla, F.J. Yu, W.Z. Zhou, P. Joseph, P. Cumpson, P. Papakonstantinou, J. Mater. Chem. A 2 (2014) 14493–14501.

[6] S. Yang, W.B. Yue, J. Zhu, Y. Ren, X.J. Yang, Adv. Funct. Mater. 23 (2013) 3570–3576.

[7] R. Lin, W.B. Yue, F.Z. Niu, J. Ma, Electrochim. Acta 205 (2016) 85–94.

[8] M.V. Reddy, G.V. Subba Rao, B.V.R. Chowdari, Chem. Rev. 113 (2013) 5364–5457.

[9] S.-S. Yang, L.-Y. Lin, X. Li, C.-W. Ma, H.-X. Lai, L.-Y. Lin, J. Energy Storage 14 (2017) 112–124.

[10] D.J. Du, W.B. Yue, X.L. Fan, K. Tang, X.J. Yang, Electrochim. Acta 194 (2016) 17–25.

[11] C.H. Chen, P.J. Perdomo, M. Fernandez, A. Barbeito, C.L. Wang, J. Energy Storage 8 (2016) 198–204.

[12] L. Zhao, M.M. Gao, W.B. Yue, Y. Jiang, Y. Wang, Y. Ren, F.Q. Hu, ACS Appl. Mater. Interfaces 7 (2015) 9709−9715.

[13] A. Ambrosi, C.K. Chua, A. Bonanni, M. Pumera, Chem. Rev. 114 (2014) 7150–7188.

[14] N.G. Shang, P. Papakonstantinou, S. Sharma, G. Lubarsky, M. Li, D.W. McNeill, A.J. Quinn, W.Z. Zhou, R. Blackley, Chem. Commun. 48 (2012) 1877–1879.

[15] S. Karamat, S. Sonuşen, Ü. Çelik, Y. Uysallı, E. Özgönül, A. Oral, Prog. Nat. Sci.-Mater. 25 (2015) 291–299.

[16] X.L. Li, H.L. Wang, J.T. Robinson, H. Sanchez, G. Diankov, H.J. Dai, J. Am. Chem. Soc. 131 (2009) 15939–15944.

[17] H. Turgut, Z.R. Tian, F.J. Yu, W.Z. Zhou, J. Phys. Chem. C 121 (2017) 5829–5835.

[18] N. Mahmood, C.Z. Zhang, H. Yin, Y.L. Hou, J. Mater. Chem. A 2 (2014) 15–32.

[19] V. Georgakilas, J.N. Tiwari, C. Kemp, J.A. Perman, A.B. Bourlinos, K.S. Kim, R. Zboril, Chem. Rev. 116 (2016) 5464–5519.

[20] C. Gómez-Navarro, R.T. Weitz, A.M. Bittner, M. Scolari, A. Mews, M. Burghard, K. Kern, Nano Lett. 7 (2007) 3499–3503.

[21] S. Yang, S. Brüller, Z.S. Wu, Z.Y. Liu, K. Parvez, R.H. Dong, F. Richard, P. Samorì, X.L. Feng, K. Müllen, J. Am. Chem. Soc. 137 (2015) 13927–13932.

[22] S. Yang, M.R. Lohe, K. Müllen, X.L. Feng, Adv. Mater. 28 (2016) 6213–6221.

[23] W. Wei, G. Wang, S. Yang, X.L. Feng, K. Müllen, J. Am. Chem. Soc. 137 (2015) 5576–5581.

[24] W.Y. Zhang, Y. Zeng, N. Xiao, H.H. Hng, Q.Y. Yan, J. Mater. Chem. 22 (2012) 8455–8461.

[25] B. Zhao, L. Jiang, X.L. Zeng, K. Zhang, M.M.F. Yuen, J.B. Xu, X.Z. Fu, R. Sun, C.P. Wong, J. Mater. Chem. A 4 (2016) 14595–14604.

[26] Z.Y. Xia, D. Wei, E. Anitowska, V. Bellani, L. Ortolani, V. Morandi, M. Gazzano, A. Zanelli, S. Borini, V. Palermo, Carbon 84 (2015) 254–262.

[27] Y. Hou, M.R. Lohe, J. Zhang, S.H. Liu, X.D. Zhuang, X.L. Feng, Energy Environ. Sci. 9 (2016) 478–483.

[28] S.S. Tao, W.B. Yue, M.Y. Zhong, Z.J. Chen, Y. Ren, ACS Appl. Mater. Interfaces 6 (2014) 6332−6339.

[29] W.S. Hummers, R.E. Offeman, J. Am. Chem. Soc. 80 (1958) 1339–1339.

[30] R.J. Li, K. Parvez, F. Hinkel, X.L. Feng, K. Müllen, Angew. Chem. Int. Ed. 52 (2013) 5535–5538.

[31] W.B. Yue, S.H. Jiang, W.J. Huang, Z.Q. Gao, J. Li, Y. Ren, X.H. Zhao, X.J. Yang, J. Mater. Chem. A 1 (2013) 6928–6933.

[32] L. Shang, T. Bian, B.H. Zhang, D.H. Zhang, L.-Z. Wu, C.-H. Tung, Y.D. Yin, T.R. Zhang, Angew. Chem. Int. Ed. 53 (2014) 250–254.

[33] P. Zhao, W.B. Yue, X. Yuan, H.Y. Bao, Electrochim. Acta 225 (2017) 322–329.

[34] Q.S. Huang, G. Wang, L.W. Guo, Y.P. Jia, J.J. Lin, K. Li, W.J. Wang, X.L. Chen, Small 7 (2011) 450–454.

[35] J.H. Warner, M.H. Rümmeli, L. Ge, T. Gemming, B. Montanari, N.M. Harrison, B. Büchner, G.A.D. Briggs, Nat. Nanotechnol. 4 (2009) 500–504.

[36] G.G. Eshetu, M. Armand, B. Scrosati, S. Passerini, Angew. Chem. Int. Ed. 53 (2014) 13342–13359.

[37] R.Z. Hu, D.C. Chen, G. Waller, Y.P. Ouyang, Y. Chen, B.T. Zhao, B. Rainwater, C.H. Yang, M. Zhu, M.L. Liu, Energy Environ. Sci. 9 (2016) 595–603.

[38] S.T. Liu, W.B. Yue, C. Zhang, D.J. Du, X.J. Yang, J. Alloy. Compd. 769 (2018) 293–300.

[39] S.B. Yang, X.L. Feng, S. Ivanovici, K. Müllen, Angew. Chem. Int. Ed. 49 (2010) 8408–8411.

[40] K. Parvez, Z.-S. Wu, R.J. Li, X.J. Liu, R. Graf, X.L. Feng, K. Müllen, J. Am. Chem. Soc. 136 (2014) 6083–6091.

[41] B.L. Caetano, F. Meneau, C.V. Santilli, S.H. Pulcinelli, M. Magnani, V. Briois, Chem. Mater. 26 (2014) 6777–6785.

[42] J.F. Yao, D. Li, X.Y. Zhang, C.H. Kong, W.B. Yue, W.Z. Zhou, H.T. Wang, Angew. Chem. Int. Ed. 47 (2008) 8397–8399.

[43] W.Z. Zhou, Adv. Mater. 22 (2010) 3086–3092.

[44] G.M. Zhou, D.-W. Wang, L.-C. Yin, N. Li, F. Li, H.-M. Cheng, ACS Nano 6 (2012) 3214–3223.

Figure Captions

Fig. 1. (a) SEM image of EEG. (b) Photographic illustration of EEG in DMF, EEG in H_2O and GO in H_2O. (c) XRD patterns of rGO-SnO_2 and EEG-SnO_2. The peaks are indexed to the tetragonal structure of SnO_2. (d) SEM, (e) TEM and (f) HRTEM images of EEG-SnO_2.

Fig. 2. HRTEM images of (a) EEG-SnO_2 and (b) rGO-SnO_2 with a SnO_2 crystallite at the top-right corner. (c) FT-IR, (d) XPS survey, (e) high-resolution C 1s XPS and (f) Raman spectra of rGO-SnO_2 and EEG-SnO_2.

Fig. 3. (a) CV curve of EEG-SnO_2 at a scan rate of 0.5 mV s^{-1}. (b) Cycle performance of rGO-SnO_2 and EEG-SnO_2 at 0.1 C. (c) Rate performances of rGO-SnO_2 and EEG-SnO_2 at 0.1–2 C. (d) The electrochemical impedance spectra of rGO-SnO_2 and EEG-SnO_2 after 3 cycles. The inset of (d) is the Randles equivalent circuit for rGO-SnO_2 and EEG-SnO_2.

Fig. 4. SEM and TEM images of (a, b) EEG-SnO_2-M and (c, d) EEG-SnO_2-H. Raman spectra of (e) rGO-SnO_2-M, EEG-SnO_2-M, and (f) rGO-SnO_2-H, EEG-SnO_2-H.

Fig. 5. Cycle performance of (a) EEG/rGO-SnO_2-M and (d) EEG/rGO-SnO_2-H at 0.1 C. Rate performances of (b) EEG/rGO-SnO_2-M and (e) EEG/rGO-SnO_2-H at 0.1–2 C. The electrochemical impedance spectra of (c) EEG/rGO-SnO_2-M and (f) EEG/rGO-SnO_2-H after 3 cycles.

Fig. 6. SEM images of (a) EEG-SnO_2-NW and (b) EEG-SnO_2-LT. (c) XRD patterns and (d) TGA curves of EEG-SnO_2-NW and EEG-SnO_2-LT.

Fig. 7. Schematic illustration of the proposed formation mechanism of SnO_2 nanocrystals on the EEG surface. (a) Polymerized precursor molecules. (b) An aggregate of the polymerized precursor molecules on the EEG surface. (c) A SnO_2 nanocrystallite developed in a disordered aggregate.

Figures

Fig. 1.

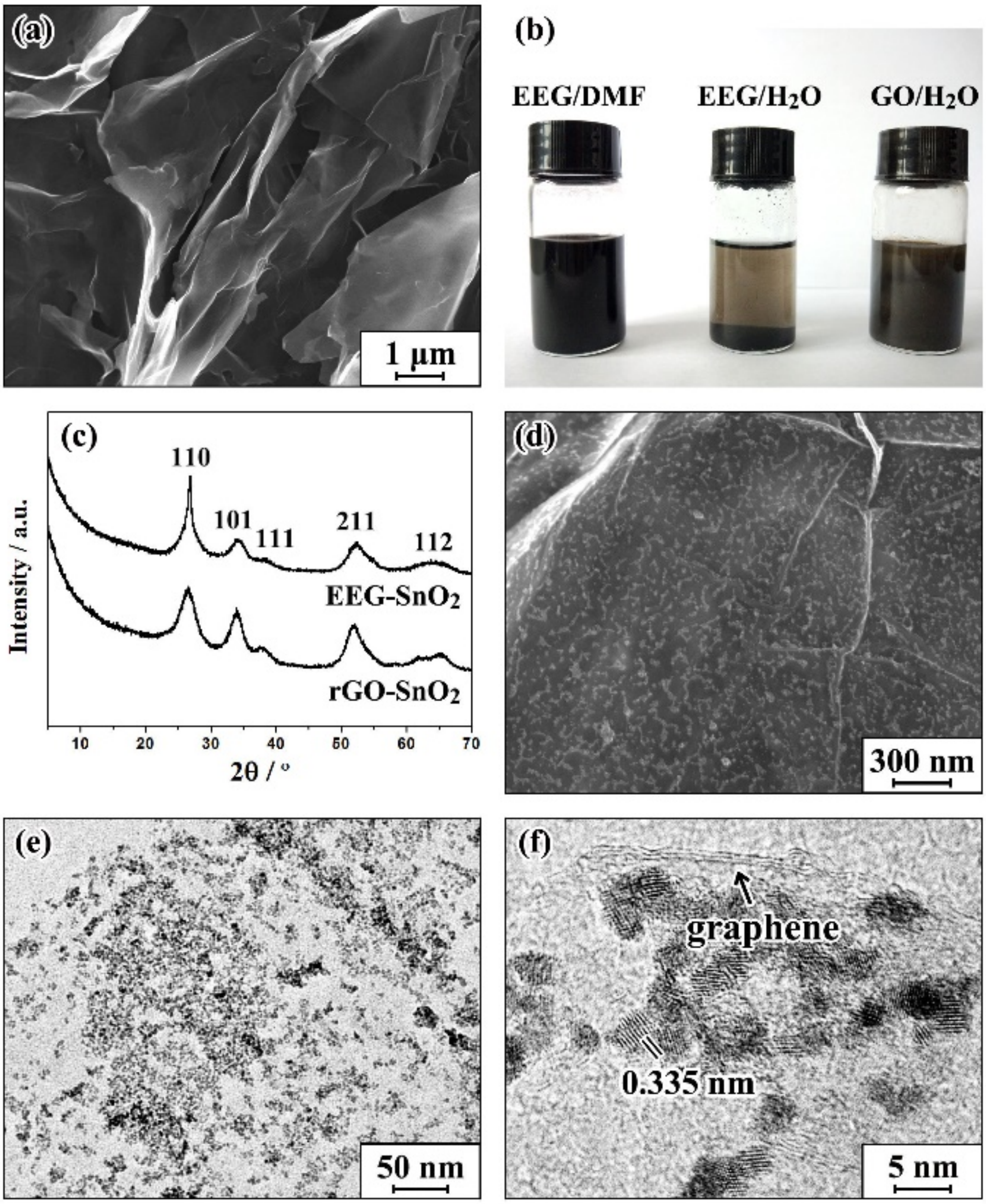

Fig. 2.

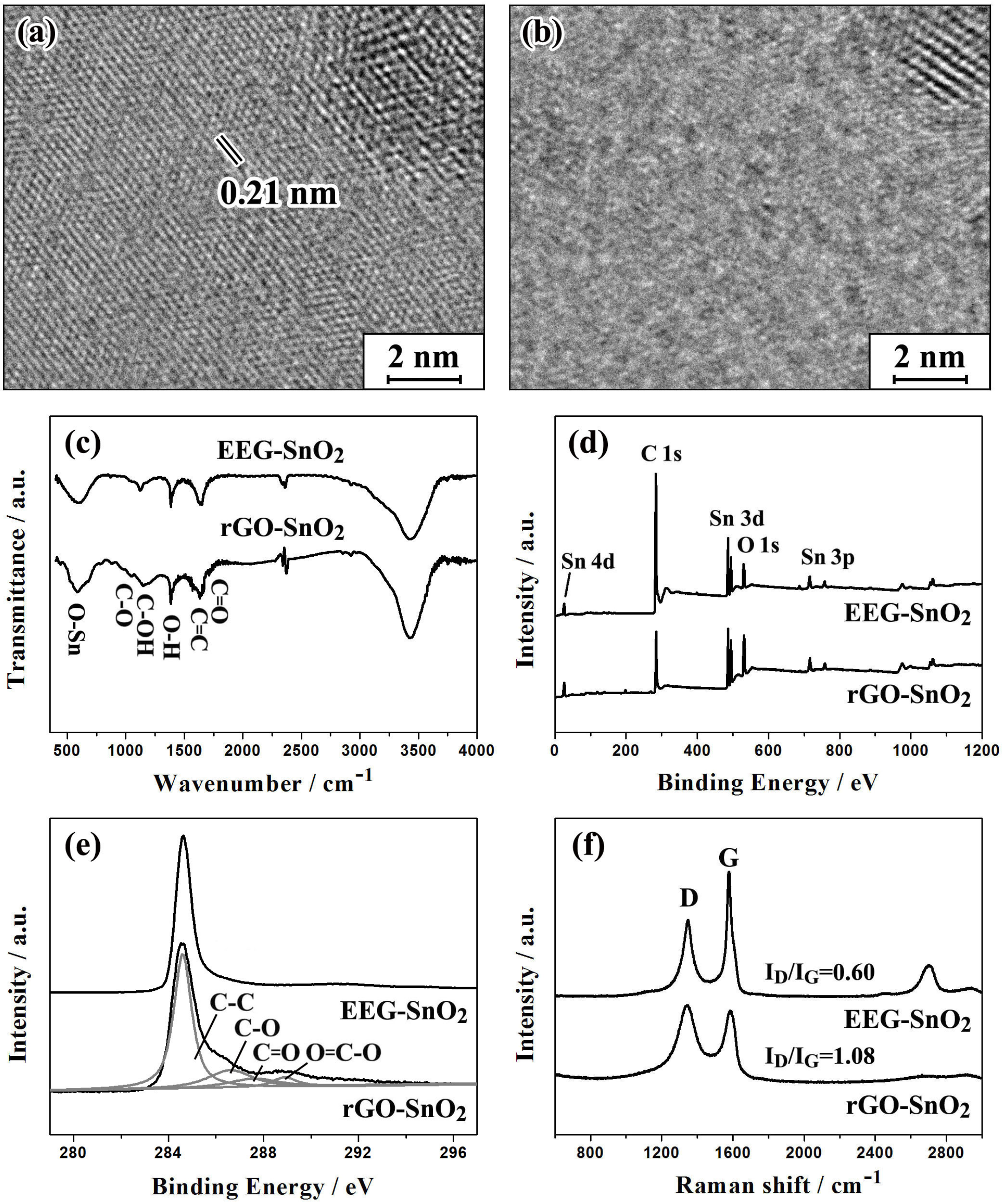
(a)
0.21 nm
2 nm
(b)
2 nm
(c)
EEG-SnO$_2$
rGO-SnO$_2$
O-Sn
C-O
C-OH
O-H
C=C
C=O
Transmittance / a.u.
500 1000 1500 2000 2500 3000 3500 4000
Wavenumber / cm^{-1}
(d)
C 1s
Sn 3d
O 1s
Sn 4d
Sn 3p
EEG-SnO$_2$
rGO-SnO$_2$
Intensity / a.u.
0 200 400 600 800 1000 1200
Binding Energy / eV
(e)
C-C
C-O
C=O
O=C-O
EEG-SnO$_2$
rGO-SnO$_2$
Intensity / a.u.
280 284 288 292 296
Binding Energy / eV
(f)
D
G
I_D/I_G=0.60
EEG-SnO$_2$
I_D/I_G=1.08
rGO-SnO$_2$
Intensity / a.u.
800 1200 1600 2000 2400 2800
Raman shift / cm^{-1}

Fig. 3.

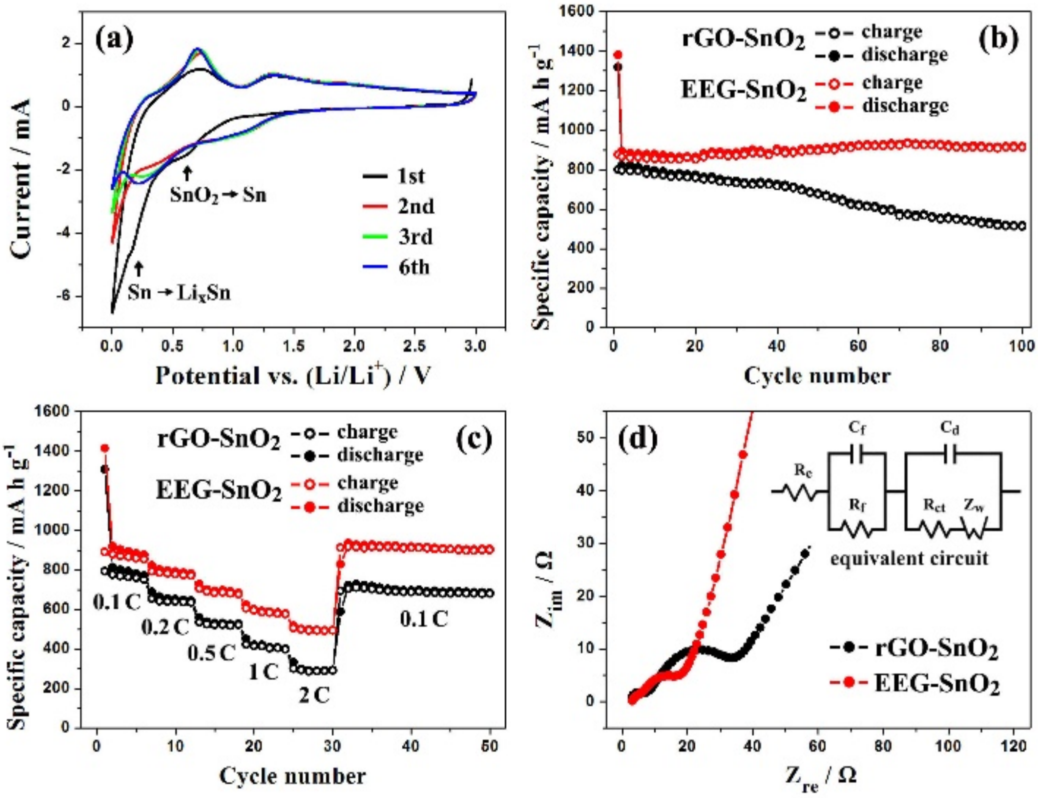
(a)
Current / mA
Potential vs. (Li/Li$^+$) / V
1st
2nd
3rd
6th
$SnO_2 \rightarrow Sn$
$Sn \rightarrow Li_xSn$
2
0
-2
-4
-6
0.0
0.5
1.0
1.5
2.0
2.5
3.0
(b)
Specific capacity / mA h g^{-1}
Cycle number
rGO-SnO_2
charge
discharge
EEG-SnO_2
charge
discharge
0
200
400
600
800
1000
1200
1400
1600
0
20
40
60
80
100
(c)
Specific capacity / mA h g^{-1}
Cycle number
rGO-SnO_2
charge
discharge
EEG-SnO_2
charge
discharge
0.1 C
0.2 C
0.5 C
1 C
2 C
0.1 C
0
200
400
600
800
1000
1200
1400
1600
0
10
20
30
40
50
(d)
Z_{im} / Ω
Z_{re} / Ω
C_f
C_d
R_e
R_f
R_{ct}
Z_w
equivalent circuit
rGO-SnO_2
EEG-SnO_2
0
10
20
30
40
50
0
20
40
60
80
100
120

Fig. 4.

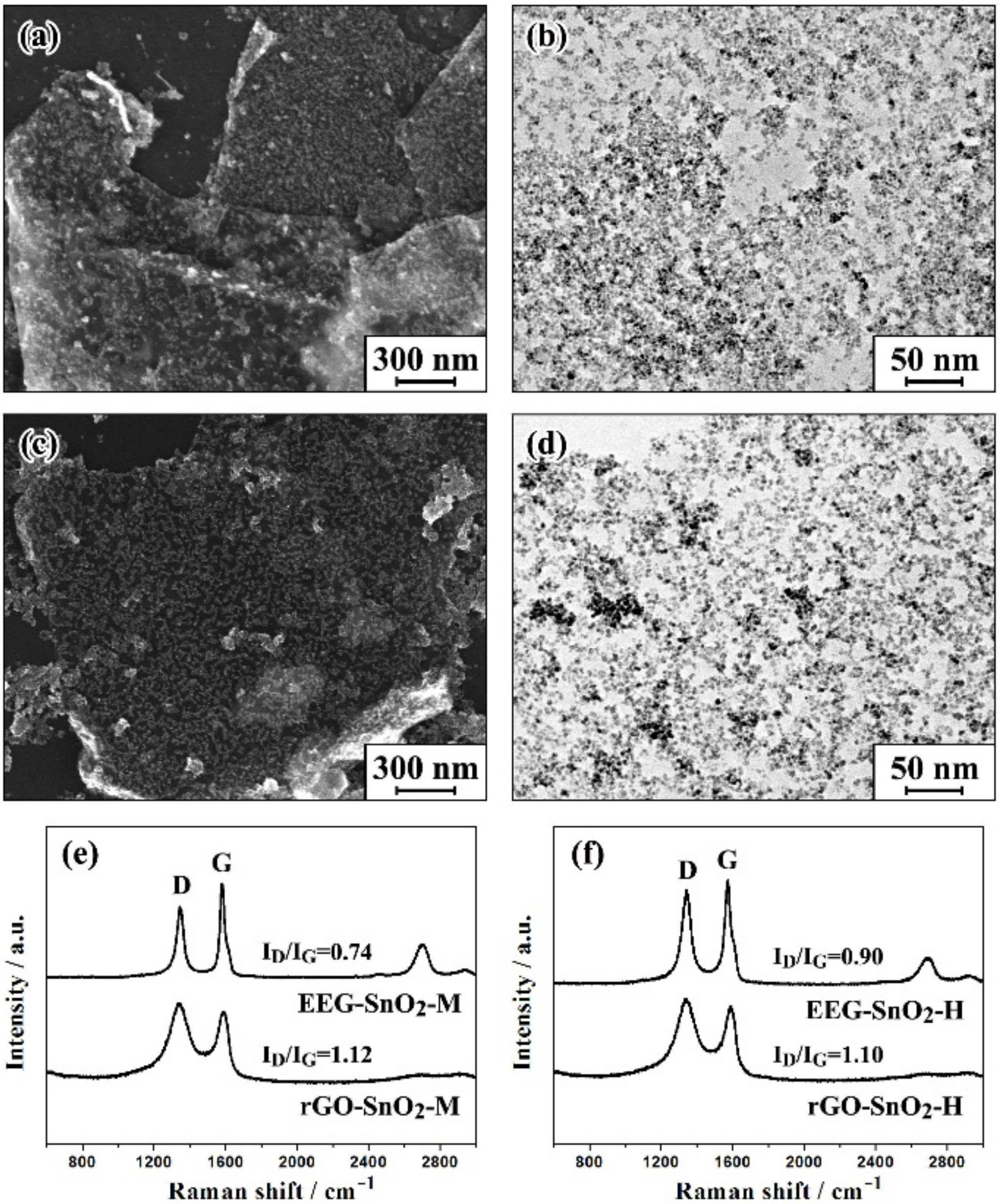
(a)
300 nm
(b)
50 nm
(c)
300 nm
(d)
50 nm
(e)
D
G
I_D/I_G=0.74
EEG-SnO2-M
I_D/I_G=1.12
rGO-SnO2-M
Intensity / a.u.
800
1200
1600
2000
2400
2800
Raman shift / cm-1
(f)
D
G
I_D/I_G=0.90
EEG-SnO2-H
I_D/I_G=1.10
rGO-SnO2-H
Intensity / a.u.
800
1200
1600
2000
2400
2800
Raman shift / cm-1

Fig. 5.

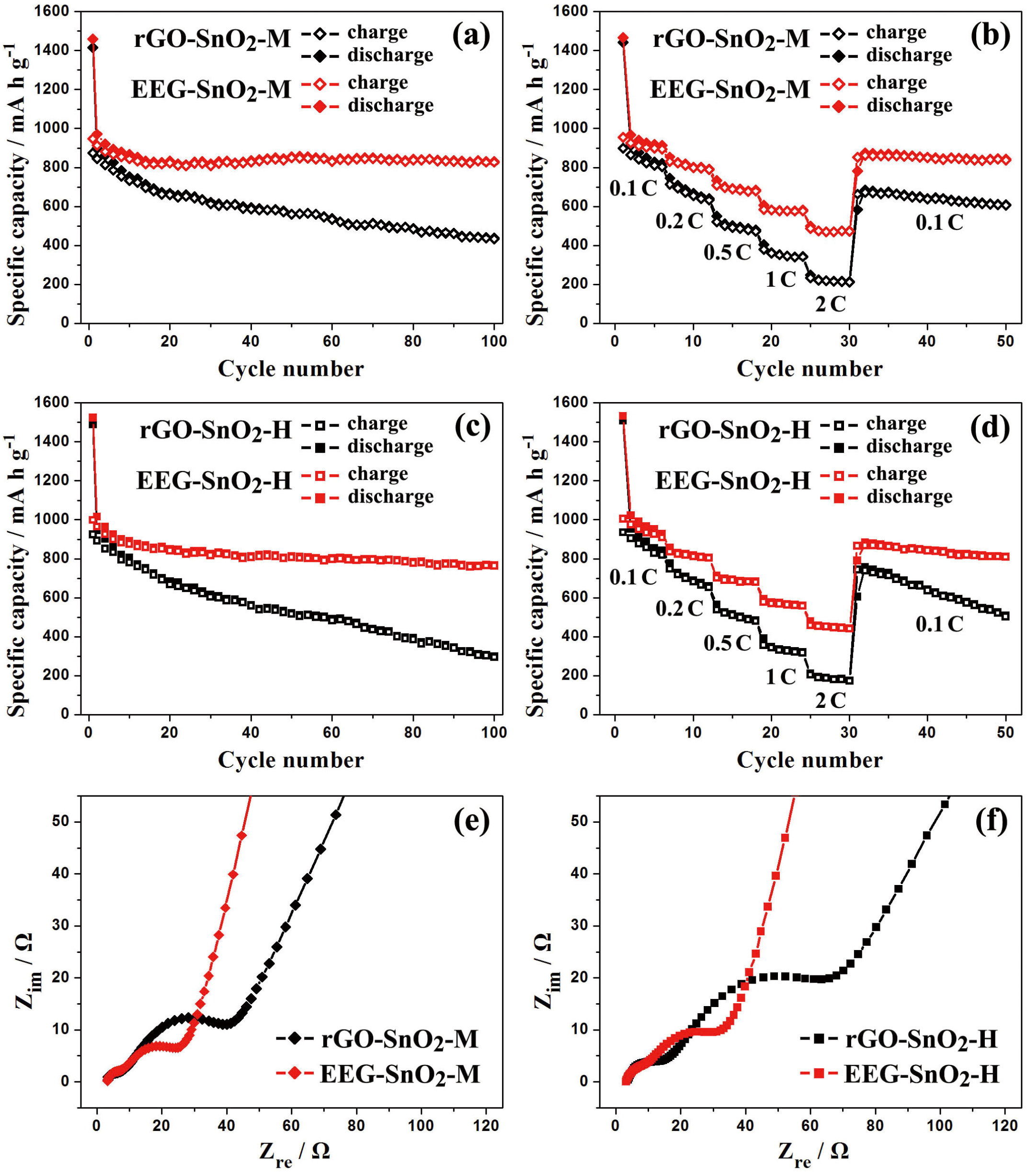
(a)
rGO-SnO2-M
charge
discharge
EEG-SnO2-M
charge
discharge
Specific capacity / mA h g-1
0
200
400
600
800
1000
1200
1400
1600
Cycle number
0
20
40
60
80
100
(b)
rGO-SnO2-M
charge
discharge
EEG-SnO2-M
charge
discharge
0.1 C
0.2 C
0.5 C
1 C
2 C
0.1 C
Specific capacity / mA h g-1
Cycle number
0
10
20
30
40
50
(c)
rGO-SnO2-H
charge
discharge
EEG-SnO2-H
charge
discharge
Specific capacity / mA h g-1
Cycle number
(d)
rGO-SnO2-H
charge
discharge
EEG-SnO2-H
charge
discharge
0.1 C
0.2 C
0.5 C
1 C
2 C
0.1 C
Specific capacity / mA h g-1
Cycle number
(e)
rGO-SnO2-M
EEG-SnO2-M
Zim / Ω
Zre / Ω
0
10
20
30
40
50
0
20
40
60
80
100
120
(f)
rGO-SnO2-H
EEG-SnO2-H
Zim / Ω
Zre / Ω

Fig. 6.

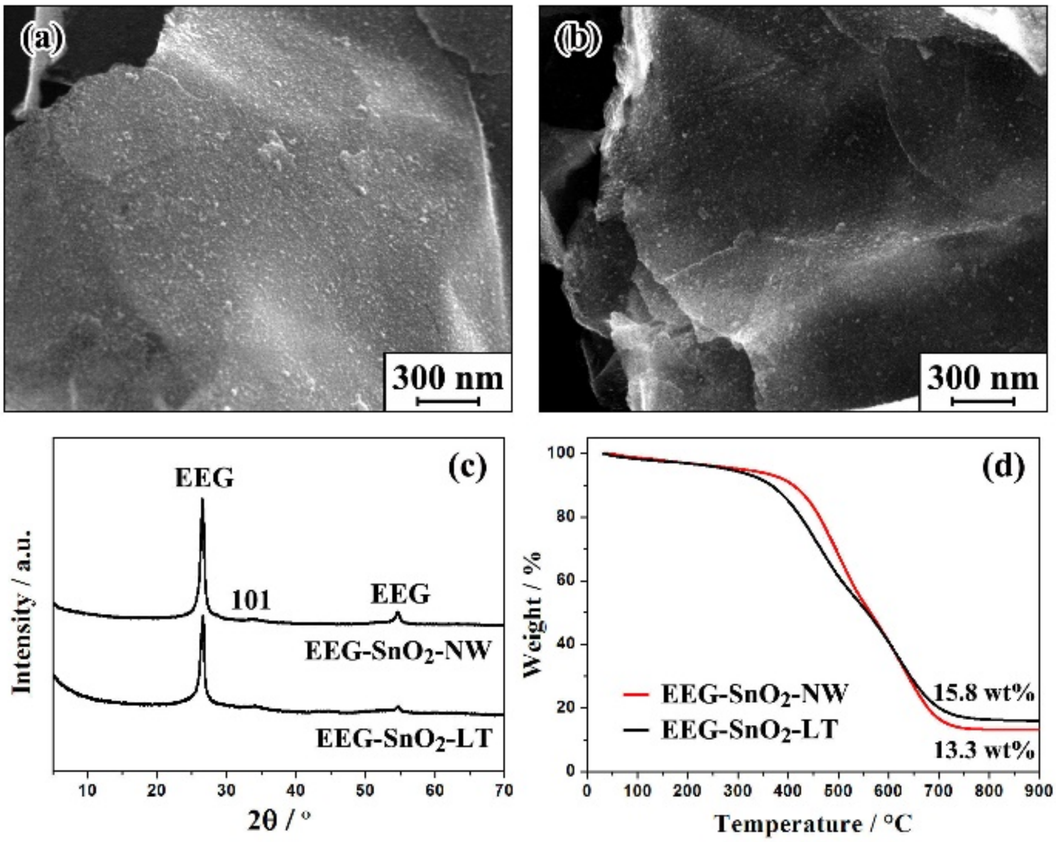
(a)
300 nm
(b)
300 nm
(c)
EEG
101
EEG
EEG-SnO$_2$-NW
EEG-SnO$_2$-LT
Intensity / a.u.
10
20
30
40
50
60
70
2θ / °
(d)
100
80
60
40
20
0
Weight / %
EEG-SnO$_2$-NW
EEG-SnO$_2$-LT
15.8 wt%
13.3 wt%
0
100
200
300
400
500
600
700
800
900
Temperature / °C

Fig. 7.

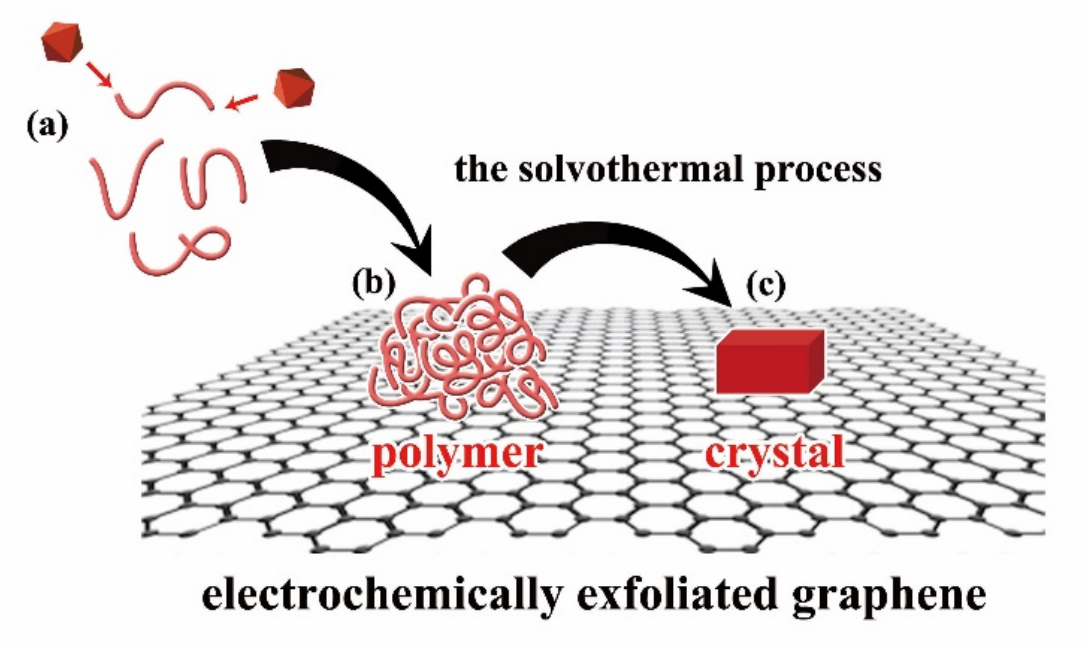
(a)
the solvothermal process
(b)
(c)
polymer
crystal
electrochemically exfoliated graphene